

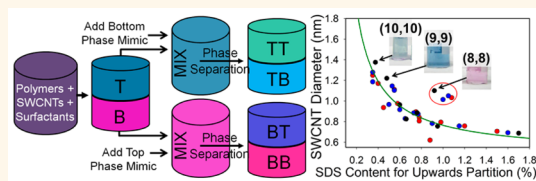


# Isolation of >1 nm Diameter Single-Wall Carbon Nanotube Species Using Aqueous Two-Phase Extraction

Jeffrey A. Fagan,<sup>\*†</sup> Erik H. Hároz,<sup>‡</sup> Rachelle Ihly,<sup>§</sup> Hui Gui,<sup>||</sup> Jeffrey L. Blackburn,<sup>§</sup> Jeffrey R. Simpson,<sup>⊥</sup> Stephanie Lam,<sup>†</sup> Angela R. Hight Walker,<sup>⊥</sup> Stephen K. Doorn,<sup>‡</sup> and Ming Zheng<sup>†</sup>

<sup>†</sup>Materials Science and Engineering Division and <sup>⊥</sup>Semiconductor and Dimensional Metrology Division, National Institute of Standards and Technology, Gaithersburg, Maryland 20899, United States, <sup>‡</sup>Center for Integrated Nanotechnologies, Los Alamos National Laboratory, Los Alamos, New Mexico 87545, United States, <sup>§</sup>National Renewable Energy Laboratory, Golden, Colorado 80401, United States, and <sup>||</sup>Department of Chemical Engineering and Materials Science, University of Southern California, Los Angeles, California 90089, United States

**ABSTRACT** In this contribution we demonstrate the effective separation of single-wall carbon nanotube (SWCNT) species with diameters larger than 1 nm through multistage aqueous two-phase extraction (ATPE), including isolation at the near-monochiral species level up to at least the diameter range of SWCNTs synthesized by electric arc synthesis (1.3–1.6 nm). We also demonstrate that refined species are readily obtained from both the metallic and semiconducting subpopulations of SWCNTs and that this methodology is effective for multiple SWCNT raw materials. Using these data, we report an empirical function for the necessary surfactant concentrations in the ATPE method for separating different SWCNTs into either the lower or upper phase as a function of SWCNT diameter. This empirical correlation enables predictive separation design and identifies a subset of SWCNTs that behave unusually as compared to other species. These results not only dramatically increase the range of SWCNT diameters to which species selective separation can be achieved but also demonstrate that aqueous two-phase separations can be designed across experimentally accessible ranges of surfactant concentrations to controllably separate SWCNT populations of very small (~0.62 nm) to very large diameters (>1.7 nm). Together, the results reported here indicate that total separation of all SWCNT species is likely feasible by the ATPE method, especially given future development of multistage automated extraction techniques.



**KEYWORDS:** single-wall carbon nanotube · separation · two-phase extraction

Separation of single-wall carbon nanotube (SWCNT) species for advanced material applications, including electronic devices<sup>1</sup> and sensor elements,<sup>2</sup> is highly desirable. For SWCNTs greater than 1.2 nm in diameter, the isolation of individual SWCNT species, and thus the achievement of refined and concentrated properties,<sup>3–5</sup> has been a particular challenge despite the development of multiple separation strategies with differing physical mechanisms in the past decade. The increased difficulty for separations of larger diameter SWCNT species can be traced to two factors: (1) the geometrically increasing number of species with similar diameters, which also implies a reduction in number fraction for any single species in a non-selective synthesis method produced sample, and (2) the generally presumed reduced difference in nanotube properties between species for larger diameter SWCNTs. The

latter effect is thought to result from a larger radius of curvature for the carbon lattice, decreasing both differentiation in the electronic structure with the specific chiral vector and likely the specificity of coating by dispersant molecules. As all commercial sources of SWCNTs are inherently polydisperse (in that they contain multiple species of nanotubes, which are typically denoted by the  $(n,m)$  indices that define the rolling vector for the carbon shell), the availability of effective separation methods to narrow or achieve individualized species distributions is necessary to refine the optical, mechanical, and electrical properties for applications. In this work, aqueous two-phase extraction (ATPE)<sup>6,7</sup> utilizing a simple gradient of two cosurfactants is demonstrated to resolve individual and reduced-diameter nanotube populations in the larger diameter range up to approximately 1.7 nm, although the upper limit for the

\* Address correspondence to jeffrey.fagan@nist.gov.

Received for review February 18, 2015 and accepted April 14, 2015.

Published online April 14, 2015  
10.1021/acsnano.5b01123

© 2015 American Chemical Society

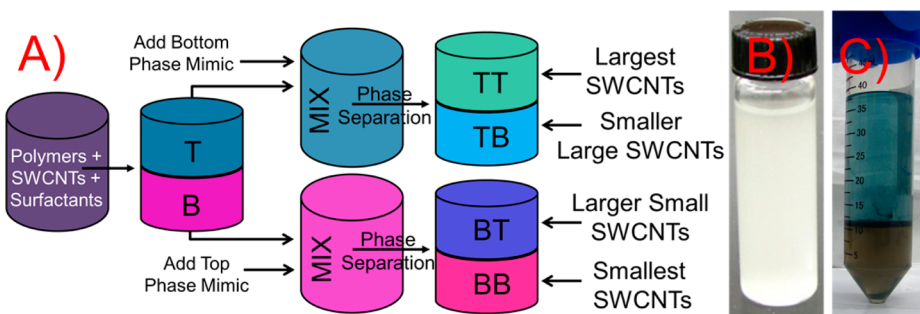


**Figure 1.** (A) Schematic of the ATPE process. A homogeneous mixture of polymers, surfactants, and SWCNTs spontaneously phase separates; individual nanotube species partition between the two phases on the basis of their individual affinities for each phase. Multiple stages of separation can be performed by pipetting the separated phases into different containers and adding aliquots of the opposite phase (“mimic phase”, prepared separately without nanotubes) containing a different concentration of surfactants. The spontaneous phase separation at each stage spatially distributes the SWCNTs on the basis of their partition coefficients at the set component concentrations. For separation on the basis of diameter as described in this contribution (two stages of separation pictured), the largest diameter SWCNTs will generally end up in the top–top (TT) fraction, followed by increasingly smaller diameter SWCNTs in the top–bottom (TB), bottom–top (BT), and bottom–bottom (BB) phases. (B) Photograph of a spontaneously separating mixture of polymers and surfactants (no SWCNTs) immediately after mixing. (C) Photograph of SWCNT partitioning after phase separation; the color difference indicates the selective partition of different (*n,m*) species into the top and bottom phases.

method is likely beyond this value. The ATPE<sup>8,9</sup> method demonstrated here has potential advantages over other SWCNT separation methods, including current industrial use for high-value macromolecules, availability of equipment for continuous processing and/or automated high-resolution extraction,<sup>10</sup> and the demonstrated ability to resolve even minor (*n,m*) species at high purities.<sup>9</sup>

## RESULTS AND DISCUSSION

The basis of the ATPE separation is the thermodynamically driven segregation of otherwise miscible and water-soluble polymers into two phases above a critical concentration threshold. Through the choice of polymer compositions, molecular weights, and variables such as pH or additive concentrations, the environment of either phase can be finely tailored to be energetically favorable for containing one or more solute species relative to the other phase. Classically this phenomenon has been used for the separation of biological macromolecules such as enzymes and proteins,<sup>11</sup> but has recently been applied successfully to SWCNTs and other nanoparticles.<sup>12</sup> In the case of SWCNTs, we have previously shown that selection by either electrical property (all SWCNT diameters) or individual (*n,m*) species in the small-diameter limit (<1 nm) was possible through the use of mixtures of bile salts,<sup>13</sup> alkyl surfactants, and iterative extraction.<sup>8–10</sup> In those works, we demonstrated high-purity resolution of 10 specific SWCNT species, the largest (by diameter) of which was the (9,4) with a carbon center to carbon center definition diameter (this diameter definition is used throughout the entirety of this study) of 0.916 nm.<sup>14</sup> Although the ATPE technique can be performed with a broad array of dispersants, including sequence-dependent extraction using single-stranded DNA oligomers and polymer systems,<sup>15</sup> in this contribution

we focus on expanding the demonstrated potential of the poly(ethylene glycol) (PEG)–Dextran 70–sodium deoxycholate (DOC)–sodium dodecyl sulfate (SDS) system we utilized in ref 9. A simplified schematic of the process is shown in Figure 1.

Herein we demonstrate the separation of individual species using nanotubes from four separate production methods: high-pressure CO disproportionation (HiPco), plasma torch (PT), laser vaporization (LV), and electric arc (EA). In order, these sources (for the materials reported) contain SWCNTs of increasingly larger average diameter, as well as different quantities and structures of residual catalyst and non-SWCNT carbonaceous impurities. Inclusively, the SWCNTs in each source were received as dry powders and bundled together in a mixture of lengths and containing varying fractions of defective, damaged, and/or open-ended nanotubes<sup>16</sup> depending on the synthesis condition and the methodology of any applied purification. To enable separation by ATPE, each of the SWCNT powders was first dispersed *via* sonication in a sodium deoxycholate solution followed by centrifugation (see Methods) to remove most non-nanotube components and larger SWCNT aggregates. This is similar to the typical preprocessing for most liquid-phase nanotube separation methods, including density gradient ultracentrifugation,<sup>17–24</sup> chromatography (ion-exchange, gel column, or size exclusion),<sup>25–32</sup> electrochemical processing,<sup>33</sup> and selective dispersion.<sup>34,35</sup> In the future, this step may be replaceable by an additional ATPE process.<sup>36</sup> For this study, an additional rate-dependent ultracentrifugation step<sup>37</sup> was applied after the typical centrifugation step to remove low-number aggregates, separate open from closed ended SWCNTs on the basis of their density, and reduce the fraction of kinked/defective nanotubes.<sup>38</sup> This step, while not necessary to enable the separations described below,

improves the clarity of the remaining nanotube optical properties and simplifies the extraction order as various removed contaminants would otherwise partition into phases with desirable species.

The absorbance spectra of the four parent SWCNT dispersions from the different SWCNT soot materials (before application of ATPE separations) are shown in Figure 2 (see Methods for preparation details). The PT, LV, and EA SWCNT populations shown in the main text are composed of empty (closed-ended) SWCNTs not containing water in their cores;<sup>23,37</sup> the HiPco SWCNT population in Figure 2 is composed of water-filled SWCNTs (open cores). Peaks in the absorbance spectra are due to the optical transitions of the individual nanotube (*n,m*) species present in each population.<sup>39</sup> Each species of nanotube has multiple major and minor excitonic optical transitions with species-dependent extinction coefficients; primary transitions most readily identified are, from lowest to greatest energy for the same SWCNT diameter, semiconducting 1–1 transition ( $S_{11}$ ), semiconducting 2–2 transition ( $S_{22}$ ), metallic 1–1 transition ( $M_{11}$ ), and semiconducting 3–3 transition ( $S_{33}$ ). Sharper (narrower line width) and taller peaks relative to the absorbance of any nonpeak absorbance are believed to indicate less defective and purer SWCNT dispersions. Many nanotube species are present in each population shown in Figure 2, but the grouping of peaks for the  $S_{11}$ ,  $S_{22}$ ,  $M_{11}$ , and  $S_{33}$  is clear (except for panel A, in which  $S_{22}$ ,  $M_{11}$ , and  $S_{33}$  overlap in wavelength). Progressing from panel A to D, the shift to lower energy of each labeled optical transition type is indicative of the increasing average SWCNT diameter across the four parent SWCNT populations.

In general, ATPE for SWCNTs is hypothesized to be governed by the relative hydrophilicity/hydrophobicity of the two polymer phases and the effective composition of the surface-adsorbed surfactant layer structure on each (*n,m*) species at the specified solution composition of all species,<sup>40</sup> although other factors can also (strongly) affect the partition.<sup>41,42</sup> This can be described most simply as an SWCNT species-dependent partition coefficient,  $k_{(n,m)}(C_{\text{surfactant}})$ , in which

$$k_{(n,m)}(C_{\text{surfactant}}) = \frac{C_{(n,m), \text{topphase}}}{C_{(n,m), \text{lowerphase}}}$$

and  $C_i$  is the concentration of the  $i$  component (e.g.,  $i = \text{surfactant}$ ,  $i = (10,9)$  SWCNT, etc.). In practice,  $k_{(n,m)}(C_{\text{surfactant}})$  is difficult to measure, as the concentration of each component affects the partition of all other components, and thus absolute partition coefficients can be determined only through direct construction of the extraction system at the desired conditions. Although measurements of the exact partition coefficient functionalities versus polymer concentration, cosurfactant concentrations, and salt conditions are ongoing (in all cases we assume that the

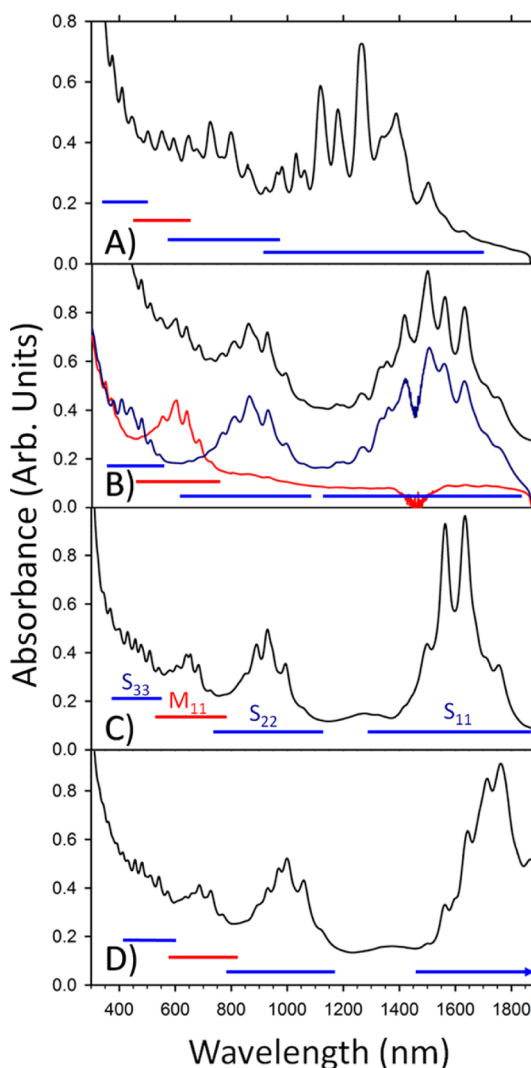


**Figure 2.** Absorbance spectra of the four prepared parent SWCNT dispersions for ATPE separation. The average diameter of the SWCNTs contained in each refined parent dispersion increases in the order (A) HiPco, (B) PT, (C) LV, and (D) EA, which is reflected in the shift of both the metallic and semiconducting optical transitions to longer wavelengths in the same order. The HiPco sample in panel A primarily contained water-filled SWCNTs. The populations in panels B, C, and D contained primarily empty (closed-ended) SWCNTs. The sharpness of the optical transitions in each spectrum is indicative that the individual SWCNTs were well dispersed. Furthermore, the intensity of the optical transitions relative to the underlying background is suggestive that relatively few impurities (except in panel B) or optically defective SWCNTs remained after population refinement. Horizontal bars marking the approximate locations of the distinct optical transitions for the semiconducting and metallic SWCNTs in each of the parent dispersions are shown in each panel; labels for the bars are shown in panel C. That the wavelengths for these transition types overlap can be seen in the bars and in the spectra of separated metallic (red curve) and semiconducting (blue curve) daughter populations for the PT SWCNTs in panel B.

nanotube concentration does not affect the phase compositions), effective partition coefficients can be readily constructed, assuming all surfactant components distribute volumetrically, and that the separate polymer phase compositions are unaffected by

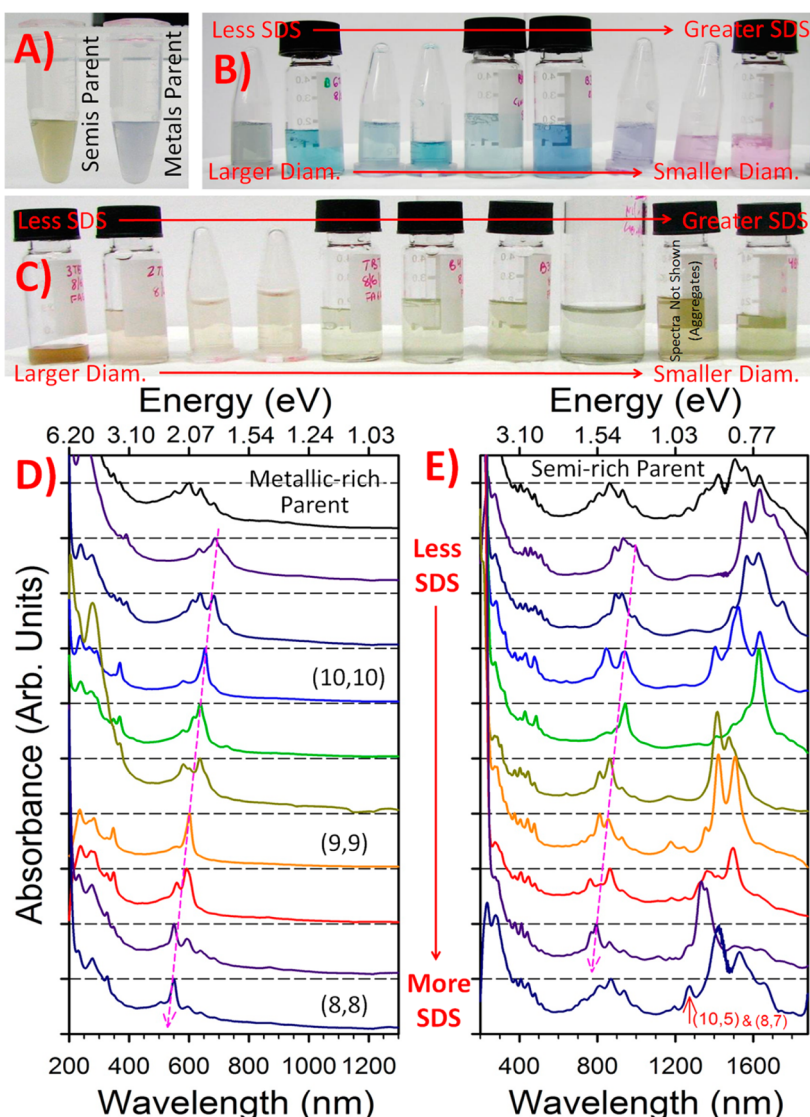
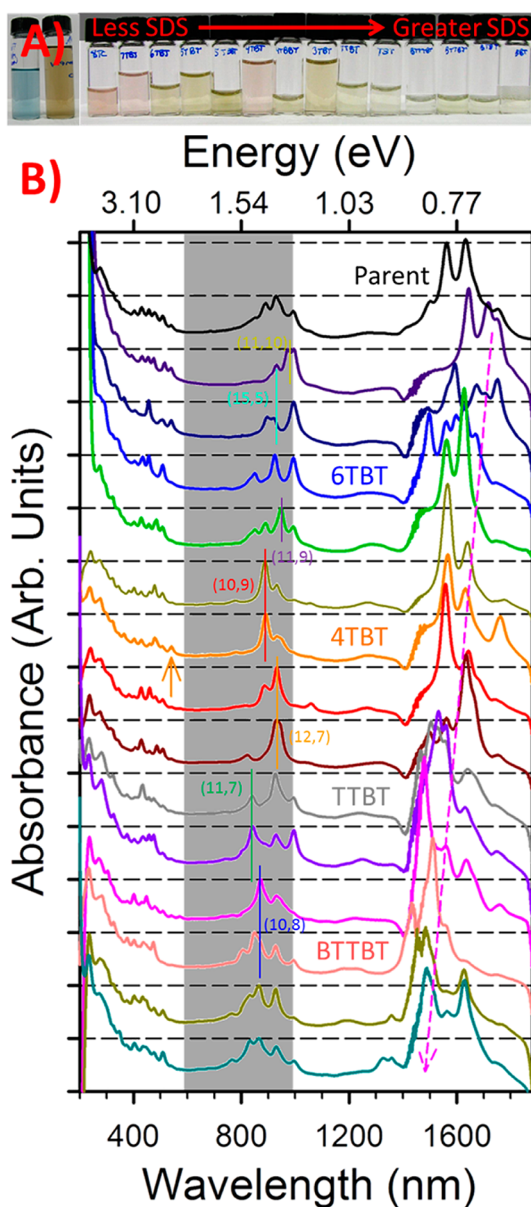


**Figure 3.** (A) Photograph of semiconducting and metallic separated empty PT SWCNT parent dispersion without diameter sorting. (B and C) Photographs of SDS gradient ATPE-separated metallic (B) and semiconducting (C) fractions from left (lowest SDS concentration for extraction) to right (greatest SDS for extraction); clear color changes are more apparent for the metallic species than the semiconductors due to the wavelength range of human visual acuity. (D and E) Absorbance spectra of shown metallic and semiconducting SWCNT fractions, respectively, in order of their appearance in the photographs. High resolution of specific diameters is especially visible in the metallic fractions due to the stronger direct correlation of diameter and optical transition wavelength for metallic SWCNTs. The central green trace in panel E is consistent with the (11,9) species. The bottom semiconducting fraction contains primarily aggregates, but also contains the (10,5) and (8,7), which require an unusually large SDS concentration for extraction (*vide infra*).

surfactant concentration. These effective partition coefficients are determined by sequential extraction of  $(n,m)$  species from the initial SWCNT population utilizing additive polymer phase mimic mixtures and assuming volumetric distribution of the non-nanotube components.

An example sequential extraction experiment utilizing mimic phase stock solutions (see Methods) is shown in Figure 3A–E for the PT nanotube dispersion. To better demonstrate the diameter-based separation that is the thrust of this contribution, the parent PT SWCNT dispersion was first separated on the basis of metallicity (Figure 3A). Of note is that in this process a

significant amount of hydrophobic, non-nanotube, impurities were removed (compare the black parent spectrum to the two daughter spectra (red/blue) in Figure 2B; a significant UV-absorbing component was removed in the metal/semiconducting separation), which contributed to the background absorbance in Figure 2B but not to the SWCNT peak feature absorbance (a similar observation was made in ref 36). A second example is shown in Figure 4 and Figure 5 for the LV nanotube parent, and a third in Figure 7 for the EA nanotube parent. Significant additional data, including spectra of diameter-separated HiPco semiconducting and metallic species (parent dispersion spectrum in



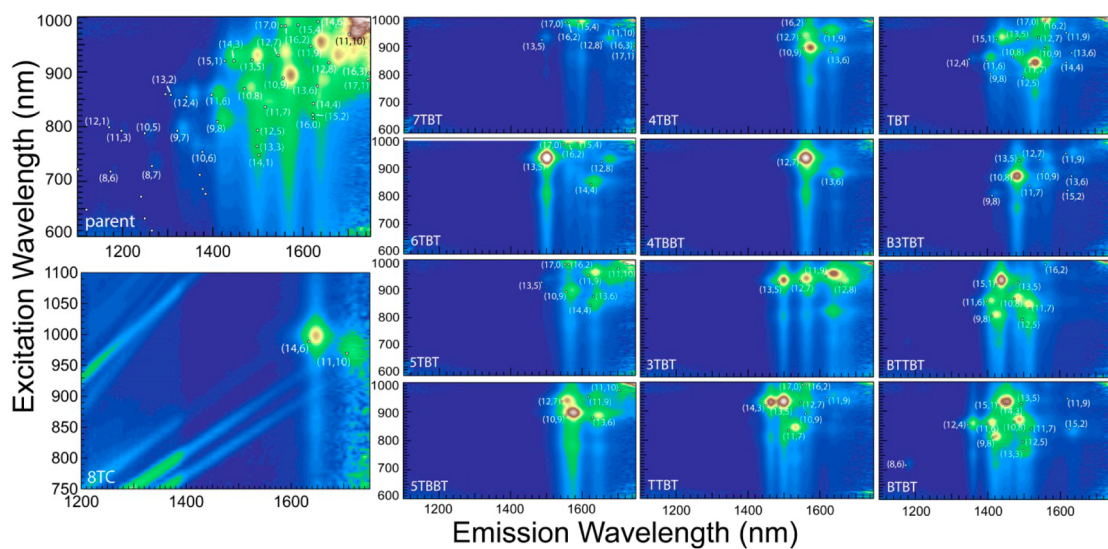
**Figure 4.** (A) Photograph of metallic and semiconducting separated empty LV SWCNTs prior to diameter sorting and of the SDS gradient ATPE-separated semiconducting fractions from left (lowest SDS for extraction) to right (greatest SDS for extraction). (B) Absorbance spectra of the sorted semiconducting SWCNT fractions in order of their appearance in the photograph in panel A (left most = penultimate top). The topmost spectrum is of the semiconducting parent dispersion shown in A. Significant variation in SWCNT species distribution occurs on the basis of ATPE separation, as demonstrated by the changes in absorbance peak wavelengths. Several peaks are identified to particular SWCNT species; an orange arrow indicates the absorbance feature that leads fraction 4TBT, and not its neighboring fractions, to be pink in color.

Figure 2A) and of ATPE separations on water-filled SWCNTs from the PT and EA synthetic sources, are shown in the Supporting Information (SI). Data for the HiPco parent dispersion are shown in the SI because relatively few of the SWCNT species in that population are  $>1$  nm in diameter, and the larger SWCNTs' overlap

in diameter distribution with the PT sample that we show can be well resolved by ATPE (*vide infra*). In all cases, for notation on extracted fractions we utilize "T" to indicate a fraction extracted from the top, PEG-rich, phase and "B" for fractions extracted from the bottom, dextran-rich, phase at each step. We furthermore annotate these notations sequentially; for example, the fraction "6TBT" indicates a fraction that partitioned six times into the top phase, then once into the bottom phase, then finished in the top phase (8 separate extractions); the notation "C" refers to "collapse" of a top phase by the addition of a small aliquot of high-concentration DOC solution, which can be used to collect all SWCNTs from a large-volume top phase into a small volume of bottom phase.

For each of the initial diameter populations (Figure 3, Figure 4, Figure 7, and Figures S2–S11) one key observation is the general monotonic trend in the energy (wavelength) ranges for the optical transitions across the sequential extractions with increasing (or decreasing) SDS content; the change in the distribution of optical transitions causes the color differences immediately apparent in the photographs. The changes in color are more striking and the extraction by hand is easier for the metallic nanotubes in Figure 3 due to the fact that their optical transitions occur near the apex of human visual acuity.<sup>43,44</sup> In contrast, for semiconducting SWCNTs  $>1$  nm in diameter, only the  $S_{33}$  transitions and some  $S_{22}$  transitions are typically in the visible spectrum, and those are near the edge of the average human visual perception range. To be explicit, compare the spectra for the first four semiconducting vials in Figure 3C (orange-tinged) to those of the second set of four (yellow-green cast). It is clear from Figure 3E that the peak locations, and thus SWCNT species distribution, are significantly different in each fraction, although the color (Figure 3C) is practically unchanged (both to the naked eye and as captured by camera).

In general, the optical transitions shift to increasingly longer wavelengths for SWCNTs extracted at lower SDS concentration (purple dashed lines in Figures 3D, 3E, and 4B); that is, larger diameter ( $n,m$ ) species are extracted at lower SDS concentration when utilizing a constant DOC concentration. A near-optimal example of this is in Figure 3D for the armchair metallic species (10,10), (9,9), and (8,8), which elute in order from largest to smallest diameter with increasing SDS concentration. Because these three species all have the same chiral angle of  $30^\circ$  (the apparent "roll up" angle of the graphene lattice relative to the nanotube long axis), the wavelength of their  $M_{11}$  optical transition is monotonically correlated with their diameter,<sup>43</sup> and the correlation between SDS concentration and extracted diameter is clearly resolved. This is consistent with the trend we previously observed for small-diameter ( $<1$  nm) SWCNTs.<sup>9</sup>



**Figure 5.** Excitation–emission contour plots for the ATPE-generated LV SWCNT samples in Figure 4. The parent, semiconducting enriched, sample (upper left) displays emission from many different species of SWCNTs. Each extracted population contains markedly fewer emitting SWCNT species, and the distribution of these species (specified by dots and labels from reported peak locations) changes markedly from fraction to fraction. As expected, the diameter trend in the observed species is from larger species to smaller species when going from the 8TC to the BTBT fractions. The green angled lines in the 8TC plot are an instrumental artifact.

A similar but slightly larger average diameter SWCNT source than PT SWCNTs and one frequently used in research studies is SWCNTs produced by the LV method. Although the average diameter of LV SWCNTs can be tuned by various synthesis parameters,<sup>35</sup> for this batch it is  $\approx 1.35 \pm 0.1$  nm. This is reflected in the longer average absorption wavelength for each set of SWCNT optical transitions than in the PT sample in Figure 1. The results of ATPE separation for the semiconducting SWCNTs from this parent are shown in Figures 4 and 5, and for the metallic LV SWCNTs in the SI.

The larger average diameter of the LV SWCNTs is reflected in the color of the separated fractions in Figure 4A; multiple fractions become visibly pinkish rather than yellow or yellow-green as the shift of the optical transitions to lower energies changes the observed color. Focusing on the absorbance spectra in Figure 4B, it is again clear that the distribution of optical transitions changes dramatically from fraction to fraction. Note that due to spectral congestion many species have similar  $S_{11}$ ,  $S_{22}$ , or  $S_{33}$  transitions, but rarely are the transition wavelengths similar in all three regions. To further demonstrate the degree of separation with less hindrance from the spectral congestion in the optical absorbance measurement, near-infrared (NIR) fluorescence spectra are reported in Figure 5 for each of the ATPE fractions of Figure 4 as well as their semiconducting enriched parent dispersion. NIR fluorescence measurement of the species distribution, which is applicable only to semiconducting species, enables better resolution of the species present in each fraction because each emission feature comes from a unique  $(n,m)$ -dependent combination of excitation and emission wavelengths. The main excitation range

for the LV semiconducting SWCNT fractions is denoted in Figure 4 through gray shading.

Using the peak locations in each contour map in Figure 5 and tabulated data,<sup>14</sup> the distinct species contributing to the overlapping absorbance features in Figure 4 can be assigned, and approximate values for the average SWCNT diameter in each fraction can be calculated. We note, however, that several species seen in absorbance are not observable by our photoluminescence (PL) spectrometer because either their emission occurs at wavelengths near or beyond the long-wavelength limit of the detector, their peak excitation wavelength is  $>1000$  nm, or both. These species likely including the (15,5), (16,3), and (13,8), which appear to be present in the absorbance data, would increase the apparent average diameter of the observed species especially in the 8TC, 7TBT, and 6TBT fractions, as well as the parent sample. Instead, in the lowest SDS concentration extracted fraction, 8TC, the largest clearly observed species is the (11,10), which has a diameter of 1.444 nm (the (14,6) has a diameter of 1.411 nm).<sup>14</sup> Figure 6 shows a plot of the apparent average diameter of each fraction as calculated by different methodologies (see caption) for species observed in the fluorescence plots of Figure 5. The systematic change in apparent average diameter between fractions, highlighted by a sloped trendline, indicates clear separation across this diameter range of nanotube species. This is despite both the limitations of our instrumental observation range, which is likely reducing the observed average diameter for low SDS extracted fractions, and the known phenomena of variation in both SWCNT absorbance cross sections<sup>45</sup> and apparent quantum yield (QY) with  $(n,m)$  species.<sup>46</sup>

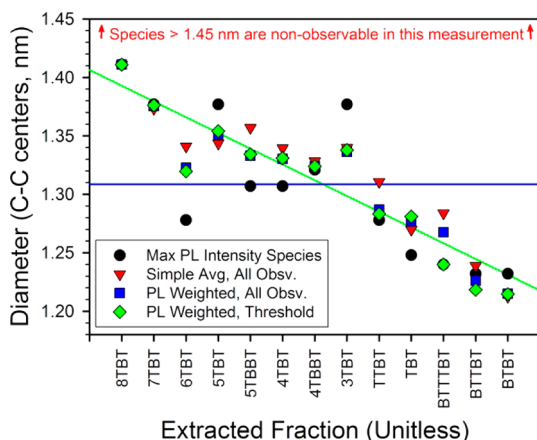


**Figure 6.** Plot of the average SWCNT diameter as determined by four different metrics for each extracted fraction from the fluorescence plots shown in Figure 5. These metrics were the diameter of the maximum intensity species, a simple average of the diameter of all observed species, an intensity-weighted average of all observed species, and a thresholded intensity-weighted average of the observed species. For the threshold averaged data set, only  $(n,m)$  species with an apparent PL intensity  $\geq 20\%$  of the highest intensity species were included in the calculation. For all metrics the trend is that larger average diameter SWCNTs were extracted to the top phase at lesser SDS concentrations; this trend is highlighted by the green eye-guide line. The average diameter of the parent sample before diameter separation, as calculated by weighting each observed species by its apparent PL intensity (no global deconvolution), is shown by the horizontal blue line. Note that several large-diameter  $(n,m)$  species observed in absorbance are not observed due to instrument limitations, which has the effect of reducing the apparent average diameter of both the parent population and especially the 8TBT, 7TBT, and 6TBT fractions.

The latter two effects, which were not considered in the calculation of the average diameter because neither factor is well characterized for most of the observed species, are reported as generally decreasing with increasing nanotube diameter for species with known values. Thus, incorporation of corrections for any of these effects would likely increase only the strength of the average diameter *versus* fraction trend reported in Figure 6.

A more commonly used and larger average diameter commercial SWCNT source than PT and LV SWCNTs is SWCNTs produced by the electric arc method. In general the average diameter of EA SWCNTs is  $\approx 1.45 \pm 0.1$  nm, which is reflected in a longer average absorption wavelength range for each set of SWCNT optical transitions than in the PT or LV samples. The results of diameter separation by ATPE for the EA SWCNTs are shown in Figure 7. In Figure 7A, the absorbance spectra of the extracted fractions continue to indicate a significant degree of separation for the large-diameter SWCNT  $(n,m)$  species present in the EA sample. This can be observed in that only rarely do the  $S_{11}$  peaks in adjacent fractions line up (note that due to the broad wavelength range of the x-axis, even very small looking shifts are  $\sim 10$  nm). The obviousness of this result is

however somewhat obscured by the increasing degree of spectral congestion across all three of the  $S_{11}$ ,  $S_{22}$ , and  $S_{33}$  optical transition ranges in the absorbance measurements and perhaps a reduction in the resolving power of the ATPE process with the particular experimental conditions chosen (addressed below). Close inspection, however, reveals that fractions with similar  $S_{22}$  peak locations display markedly different  $S_{33}$  peaks, indicating that the ATPE method continues at a minimum to generate species separation across the range of SDS concentrations employed. Unfortunately, we could not construct species/diameter distributions by measuring NIR fluorescence from these samples due to instrumental limitations (the emission wavelengths of these species are outside the detector range). Instead, we report radial breathing mode (RBM) distributions as measured at 488 and 514 nm using resonant Raman spectroscopy in Figure 7 panels C and D. Consistent with the expected diameter distribution of the parent, SWCNT species across the diameter range from approximately 1.61 nm ( $\omega_{\text{RBM}} \approx 152 \text{ cm}^{-1}$ ) to 1.31 nm ( $\omega_{\text{RBM}} \approx 185 \text{ cm}^{-1}$ ) are observed, with most observed RBM features in the range 164 to 170  $\text{cm}^{-1}$ , corresponding to a SWCNT diameter range of approximately 1.53–1.42 nm.<sup>47</sup> Ideally, we would additionally assign  $(n,m)$  indices to the observed RBM values for each fraction to identify the SWCNTs contributing absorbance peaks in each fraction. However, the paired values for  $S_{33}$  (or potentially  $S_{44}$ ) transition locations and RBM shift as a function of  $(n,m)$  are not sufficiently well known for DOC-dispersed SWCNTs with empty endohedral volumes to enable assignments. Additional Raman data on the same samples are presented in the SI.

Using spectral data from a combination of absorbance, photoluminescence, and Raman scattering methods, as well as tabulated data,<sup>14,47</sup> many of the  $(n,m)$  species contributing to each fraction can be assigned. Specific individual  $(n,m)$  species isolated at particularly high purity in Figure 3, Figure 4, and the SI include the metallic (8,8), (9,9), and (10,10) species and the (12,4), (10,9), (12,7), and (11,9) semiconducting species. Of particular interest is the degree of isolation for the two largest armchair metallic species, the (9,9) and (10,10), as there have been many theoretical and computational efforts on the (10,10) in particular<sup>48–51</sup> but few experimental samples. To evaluate the success of the ATPE process at achieving the purification of these species, we compare the RBM region Raman scattering spectra acquired near the  $M_{11}$  optical transition for each sample to that of the metallic-enriched parent from which they were isolated. These spectra are shown in Figure 8A and B. This method of comparison is important, because it is believed that Raman scattering is a much more sensitive detection method for minor impurities than absorbance or fluorescence characterization, especially when the species are close

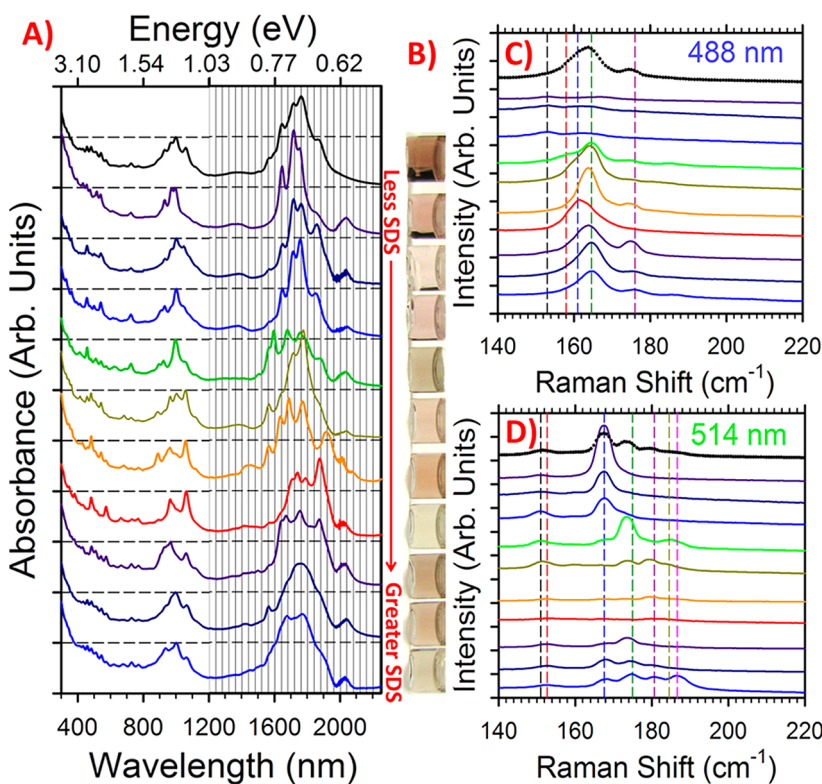


**Figure 7.** (A) Absorbance spectra of ATPE-separated empty EA semiconducting SWCNT fractions. Vertical lines in the  $S_{11}$  region are at 40 nm spacing to allow for comparison of peak locations. (B) Photographs of the parent semiconducting SWCNTs and SDS gradient separated semiconducting fractions from top (lowest SDS for extraction) to bottom (greatest SDS for extraction). Color changes mostly reflect variation in the  $S_{33}$  transition distributions due to the wavelength range of human visual acuity. (C and D) Resonance Raman spectroscopy spectra for the parent and ATPE fractions in panel A at excitation wavelengths of 488 and 514 nm in the radial breathing mode (RBM) frequency window. Colors correspond to the (same order) fractions as in the absorbance spectra. The parent sample's spectrum is shown in dots rather than a line plot to show the instrumental resolution, which changes as a function of the excitation wavelength. The intensity scale is uniform for each panel (sample absorbances were similar) to highlight that the resonant RBM peak features clearly change from fraction to fraction. This observation indicates that although spectral congestion limits our ability to distinguish the extent of separation *via* the absorbance spectra, the actual  $(n,m)$  species contributing peaks to those spectra change considerably across ATPE fractionation. Vertical dashed lines are drawn through some of the peak features to demonstrate that peak locations are distinct and different for each of the fractions.

in diameter or optical properties.<sup>52</sup> In Figure 8, both samples are demonstrated to be dramatically enriched in either the (9,9) or (10,10) SWCNT species (as appropriate) relative to the parent distribution. Note that both the (9,9) spectra for 603 nm excitation and the (10,10) spectra for 654 nm are scaled to roughly the maximal value of the parent peak by the divisor noted in the legend; the intensity scale is constant across both panels. Compared to the metal-rich parent dispersion, in both cases most of the nonarmchair metals are absent, and the fraction of the armchair species is greatly increased.

The largest diameter near monochiral species that is clearly identifiable with high confidence is the (10,10), at 1.36 nm diameter, although other groups of two to three  $(n,m)$  species all with diameters of  $>1.4$  nm are also clearly resolved (such as in the LV 8TC sample in Figure 5). Even given the high standard of isolation to the single  $(n,m)$  level, ATPE is thus demonstrated to have a significantly larger resolution range than that demonstrated for gel chromatography (GC), as the

(8,7), with  $d \approx 1.03$  nm, appears to be the largest reported isolated species in the current literature on GC separation.<sup>29</sup> Our results also demonstrate that ATPE allows resolution at diameters competitive with DGU and polyfluorene extraction. The previous record for DGU isolation of individual  $(n,m)$  species appears to be the (11,10),<sup>3</sup> with  $d \approx 1.44$  nm, or a combination of the peak positions consistent with several  $(n,m)$ 's including the (18,4), (19,2), and (20,0),<sup>5</sup>  $d \approx 1.59$  nm; polyfluorene extraction has recently demonstrated relatively high purity isolation of the (10,9) SWCNT, with  $d \approx 1.29$  nm.<sup>54</sup> Furthermore, resolution *via* ATPE of even larger diameter species ( $d > 1.4$  nm) is strongly implied in that we were able to generate different distributions of observed  $S_{11}$  and  $S_{22}$  features in Figure 7 (and as supported by the Raman data that the absorbance differences indicate different  $(n,m)$  distributions). Although we are not able to specifically quantify the change in the populations of the EA semiconducting SWCNT ATPE fractions at this time due to instrumental limitations, we note that driving visible change in the

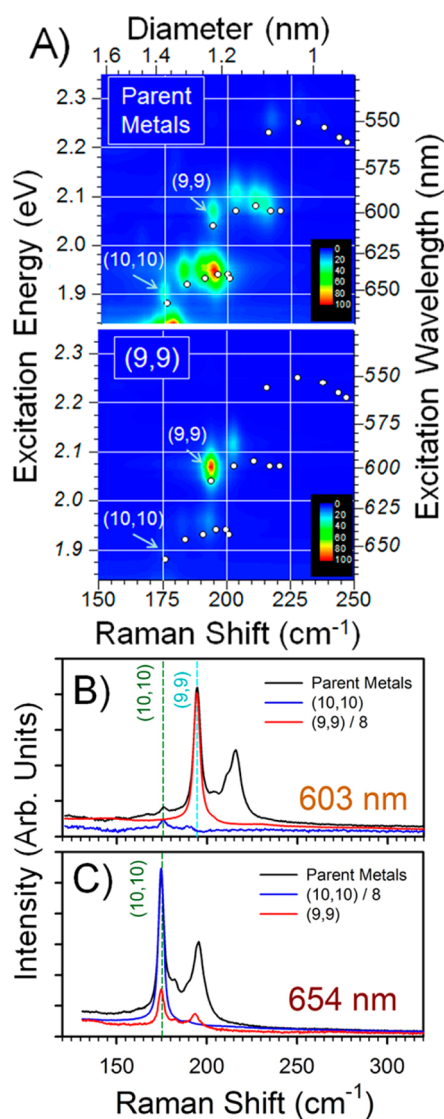


**Figure 8.** Resonant Raman scattering intensity as a function of the Raman shift for the (9,9)- and (10,10)-rich samples shown in Figure 2D, as well as for the metallic-rich parent from which they were isolated. (A) Contour plot of the Raman RBM resonance window for the metallic-rich parent and the (9,9)-enriched fraction. (B) Raman spectra of the samples with 603 nm excitation. (C) Raman spectra of the samples with 654 nm excitation. Vast enrichment in the target species is observed in both separated samples as compared to the parent distribution. Observed RBM values for both the (9,9) and (10,10), 194.4 and 175 cm<sup>-1</sup>, respectively, are consistent with literature values.<sup>47,53</sup> Although small levels of impurity species are still observed, the reader is reminded that these fractions were isolated by hand with only two intervening fractions (see Figure 3) on the basis of the observed color of the separated phases; thus, the intrinsic resolving power of the method is likely significantly greater. Note that in panels B and C the target species' intensity was divided by a factor of 8 to enable comparison of peak frequencies. Figure S10 shows the absorbance spectra of these samples at a higher level of detail than in Figure 3D.

distribution still indicates significant separation, given the geometric diameter driven increase in the number of candidate species and a limited initial sample mass constraining the number of practical ATPE steps (the yield of empty SWCNTs is roughly 1/85th the initial

mass from the utilized material after all purifications). Separate extraction experiments on water-filled CVD SWCNTs also show that improvement in the separation of these and even larger species is likely achievable by increasing the DOC concentration in the ATPE system (SI Figures S11 and S12, shown for floating catalytic decomposition (FCCD) SWCNTs).<sup>55,56</sup> In those experiments, having ~0.1% DOC as the extraction condition demonstrably allowed for significant diameter resolution of large, approximately 1.6–1.8 nm diameter SWCNTs at SDS concentrations in the 0.7–0.15% range. These results indicate that enhanced resolution is likely achievable for >1.4 nm diameter SWCNTs by increasing the DOC concentration during the separation to expand the SDS-driven partitioning window. Experiments in this direction are ongoing.

On the basis of the approximate SDS concentration (calculated using the volumetric distribution assumption) and utilizing the individuality of the nanotube optical transition wavelengths, we can estimate the SDS concentration at which the partition coefficient moves from <1 to >1 for many of the species observed in Figure 3, Figure 4, and the SI figures; we also include values for the small-diameter (*n,m*) SWCNT separation reported in ref 9. An estimate for the relative uncertainty in each SDS concentration ( $1\sigma$ ) is  $\leq 0.04\%$ , based on the nominal step size of the concentration changes applied and the repeatability of the separations. However, this estimate is limited by the unknown distribution of the surfactants within the two-phase, minor variations related to the specific lots of the chemicals used in the process and the fact that some nanotube species elute at multiple, distinct surfactant concentrations, likely due to enantiomeric effects.<sup>10</sup> A plot of SWCNT diameter for identifiable (*n,m*) species versus the estimated SDS content for extraction is presented in Figure 9.

Despite the empiricism of Figure 9, it contains valuable information about both the selectivity of nanotube species as a function of diameter and, for our identified species, an insensitivity to other nanotube characteristics such as whether the species is mod 1, mod 2, or metallic. The primary observation is that most of the plotted species fall generally onto a line described by the empirical equation  $d = 0.284 \text{ nm/SDS}(\%) + 0.48 \text{ nm}$  (EA fractions were also extracted at SDS concentrations consistent with the empirical line).

This equation can be used to estimate the resolution limit of the ATPE method in manual separations if we estimate our control of the solution conditions. If we estimate that the SDS concentration can be controlled in the multistage separation process to the level of 0.01%, then the equation predicts that ATPE (at these conditions) should be able to resolve single (*n,m*) species up to  $\approx 1.62$  nm in diameter (if we approximate that individual species are distinct by an  $a \geq 0.05$  nm difference in diameter). While it is likely that the scatter

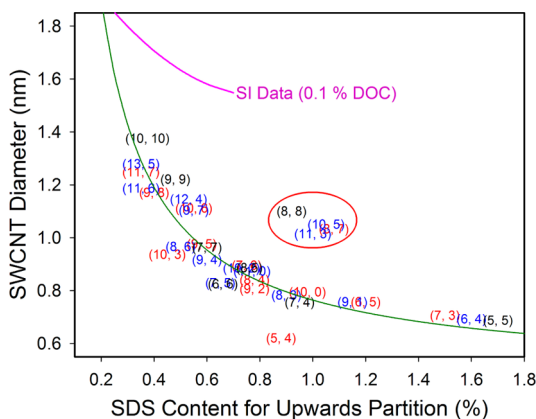


**Figure 9.** Approximate concentration of SDS required to extract specific  $(n,m)$  species of SWCNT to the PEG phase at an approximately constant DOC concentration of 0.4–0.5 g/L ( $\sim 0.045\%$ ). The SWCNT diameter (vertical axis) is the carbon centers' diameter. Label color indicates whether the species is semiconducting (red = mod1, blue = mod2 species) or metallic (black, mod0). Most nanotube species are observed to partition to the upper phase at SDS concentrations approximated by the green empirical curve  $D/\text{nm} = 0.284/(\text{SDS}/\%) + 0.48$ . Apparent outliers to this trend are visible for  $\text{SWCNTs} \approx 1.03 \text{ nm}$  in diameter (red circle) and for the (5,4). Note that the identified extraction conditions are sensitive to external factors such as polymer and cosurfactant concentrations as well as temperature and were measured for populations of unknown enantiomeric ratio. The purple empirical curve reports the approximate SDS concentration for partitioning even larger diameter nanotubes when extraction is performed at a nominal DOC concentration of 1 g/L ( $\sim 0.1\%$  DOC).

of the  $(n,m)$  species about the nominal behavior (as described by the equation) due to the specific  $(n,m)$  structure could increase or decrease this value near the resolution limit, we can still use the 1.62 nm value to estimate that species at least as large as the (14,10), with a first optical transition energy of  $\sim 0.64$  eV, should be isolatable as individual species using ATPE at a nominal DOC concentration of 0.4 g/L ( $\sim 0.04\%$ ). Advancements such as automated extraction, generating many theoretical plates of separation, would serve only to increase this resolution capability.

It is probable, however, that the DOC concentration used in the experiments of Figures 3 to 7 is not an optimal value for the separation of all SWCNT diameters. Evidence that the extraction conditions may be modifiable to increase the effective range of size discrimination can be seen through the demonstration that large-diameter SWCNTs can be separated by diameter at greater SDS concentrations with an increased DOC content. As reported above, this is the case for FCCD SWCNTs, with the estimated curve relating the extracted diameter to the SDS concentration, at a DOC concentration of 0.1%, shown in purple in Figure 9. If we hypothesize that the two cosurfactants are in competition for adsorption sites on the SWCNT interface, by increasing the DOC mass fraction we are shifting the equilibrium interfacial layer to include more DOC molecules (which in turn favors

partition into the dextran phase). This idea, and the observed curve, implies that it is possible to compensate for the reduction in diameter resolution with SDS concentration observed at 0.04% DOC by increasing the DOC concentration. Given the reduced slope of the purple curve, a much larger size limit for  $(n,m)$  resolution can be estimated using the same estimated degree of control for the SDS concentration as in the calculation based on the empirical curve for  $\sim 0.04\%$  DOC. Thus, the diameter limit for single-species resolution through ATPE separation is likely significantly larger than that initially estimated above and perhaps can be extended to other similar diameter nanotube allotropes such as double or few-wall carbon nanotubes.

Figure 9 also allows for several other important observations regarding the mechanisms underlying the ATPE extraction method. For example, there is little dependence on nanotube subtype (*i.e.*,  $\text{mod}(n-m,3) = 0, 1, 2$ ), and the order of elution is different than that observed using the gel chromatography technique with solely SDS solutions.<sup>28,29,32</sup> These two observations indicate that both the SDS and DOC surfactants actively determine the partitioning in the aqueous two-phase system, an observation highlighted by the fact that exchanging DOC for sodium cholate (SC) either eliminates separation (all nanotubes partition into the PEG-rich phase) or leads to separation on the basis of the metallic or semiconducting nature of the SWCNT.<sup>8</sup> Another interesting observation is of a clear cluster of  $(n,m)$  species (red circle in Figure 9) that partition at SDS concentrations far from the empirical curve (as well as the (5,4)). The mechanism why these species, all having diameters in the range of 1.0 to 1.1 nm, partition differently is of great interest, but is currently undetermined. We hypothesize that perhaps the packing structures of DOC molecules on SWCNT species of this size are unusually well structured and cooperatively attached, possibly leading to an exclusion of, and/or a decrease in, SWCNT surface coverage by SDS, which would inhibit partitioning into the PEG phase. This hypothesis is a clear direction for further work that can potentially be aided by such tools as analytical ultracentrifugation.<sup>57,58</sup> Differences in the effects of DOC and SC are likely related to differences in binding energy of each surfactant to the SWCNT surface, affecting accessibility for competitive adsorption of SDS or other molecules.<sup>42,58,59</sup> To also address the other significant outlier species, the (5,4), we intuit that perhaps it separates out of diameter order due to its small size (it is the smallest species we observe in commercial SWCNT materials) or perhaps due to enantiomeric effects; in some extraction experiments (not shown) fractions containing the (5,4) have also been recovered with the (6,4) species (*i.e.*, at much higher SDS concentrations). Proving the cause for either of these unusual partitioning behaviors, however, is not within the scope of this contribution.

We close by addressing the context of this work with regard to the potential for obtaining isolated SWCNT samples of narrow or monochiral (*n,m*) distribution of arbitrary diameter. Figure 9 indicates strongly that the resolution limit of the ATPE method for isolating a specific (*n,m*) SWCNT at optimized conditions is likely  $\geq 1.7$  nm, and our observation is that this method can be uniformly applied to all species without significant material loss due to processing even with many stages of extraction. Instead, the current bottleneck to generating macroscopic samples of a specific, large-diameter (*n,m*) is probably in the cost (in time and money) to the separator of isolating an SWCNT with a small fractional concentration in its initial source soot: the fractional concentration of any (*n,m*) being reduced in the initial dispersion by the increasing number of geometric (*n,m*) combinations with increasing average diameter of the parent soot (assuming nonspecific synthetic methods). This is a detriment in that the low abundance of any specific (*n,m*) will effectively set a maximum yield for that (*n,m*) from a parent soot. Additional current issues are mass losses in dispersion due to as-received material purity or morphology-driven dispersion inefficiency for some/certain morphologies of soot, the likelihood that chemical modifications alter the extraction behavior (limiting the fraction of the (*n,m*) quantity that may be collectable), and the occurrence of enantiomers potentially preventing all variants of one (*n,m*) type from separating into the same fraction. There are also limitations to the methodology employed herein (manual extraction): (1) cumulative inexactness in knowing the volumes and exact compositions of the surfactants and polymers in the two phases; (2) time limitations for how many steps are feasible (especially when targeting separate collection of all (*n,m*) species in a population); and (3)

limitations on assessing the purity of a given fraction *in situ*, as precise determination of the (*n,m*) distribution is visually challenging in the high-purity limit. Automation and scale-up of the ATPE technique, for which it is well suited, along with advancement in synthetic methods for SWCNTs, should help to alleviate these bottlenecks. These advances should enable novel technologies, as other contributions to the literature have indicated that reduced variation in SWCNT band gap and tunable absorbance wavelengths (to name a few) are desirable properties for advancing technological applications of nanotubes.<sup>60</sup>

## CONCLUSIONS

Significant extension to the demonstrated diameter range for single SWCNT species isolation *via* ATPE is presented, with nonautomated separation achieving significant resolution of narrow distribution and near-monochiral (*n,m*) species with diameters as large as or larger than those demonstrated using any other literature technique. Utilizing an empirical correlation between the extraction conditions and SWCNT diameter, a lower limit for the maximal diameter (*n,m*) species that could be isolated by hand was estimated to be  $\sim 1.6$  nm, with this value likely to be increaseable by modifying the extraction conditions. The technique was furthermore demonstrated to be applicable to SWCNTs from multiple synthetic production methods, as well as for both empty and water-filled SWCNTs from those populations. Isolation of specific (*n,m*) species concentrates spectral density in the nanotube optical features and may increase performance in SWCNT applications for which well-specified properties are desired. Automation utilizing these results may normalize the production of such materials and enable experimental evaluation of such performance.

## METHODS

Certain equipment, instruments, or materials are identified in this paper in order to adequately specify the experimental details. Such identification does not imply recommendation by the National Institute of Standards and Technology, nor does it imply the materials are necessarily the best available for the purpose. HiPco (Rice University lot 107.1r), plasma torch (Raymor Nanotech RNB-020 grade lot no. RNL13-020-016), laser vaporization (National Renewable Energy Laboratory lot Y140410), and electric arc (Carbon Solutions lot P2-200A, AP-I-043012, and AP-182) SWCNTs were procured from or donated by the manufacturer and utilized without modification. Sodium deoxycholate (BioXtra 98+%), sodium dodecyl sulfate (>99%), sodium cholate (>99%), and iodixanol (sold as Opti-Prep) were acquired from Sigma-Aldrich and used without further purification. NaClO (10–15% solution) was acquired from Sigma-Aldrich and diluted 1:99 with 18.1 MΩ H<sub>2</sub>O to generate a working NaClO stock solution. Poly(ethylene glycol) (6 kDa) was acquired from Alfa Aesar. Dextran 70 was purchased from TCI (lot no. BMGYL-TK). Initial stock solutions of PEG and dextran were prepared on a mass/mass basis, and stock surfactant solutions were prepared on a mass/volume basis; iodixanol is sold as a 60% volume fraction stock solution. All solutions prepared from

these stock solutions were prepared by volumetric dilution, with nominal concentrations estimated with respect to the volumetric ratio of the dilution.

Dispersion and pre-ATPE SWCNT purification have been reported extensively in prior work; briefly SWCNT powder (1 mg/mL) was dispersed in DOC (20 g/L) solution *via* tip sonication (30 min or 1 h, 0.9 W/mL) followed by centrifugation (Beckman J-2 centrifuge, JA-20 rotor, 1884 rad/s, 2 h) followed by collection of the supernatant. Aliquots ( $\approx 8.2$  mL) of the supernatant were then layered on top of  $\approx 28$  mL of 10% (volume/volume) iodixanol, 10 g/L DOC solution, and ultracentrifuged for 3 h in a VTi-50 rotor (Beckman-Coulter) at 5240 rad/s (50k RPM) at 20 °C. Photographs of the separated SWCNTs within the centrifuge tubes denoting the separated layers are shown in the SI. Primary bands in the middle of each centrifuge tube containing well-individualized and primarily rigid SWCNTs were collected; the top collected band has previously been shown to contain empty, closed-ended, SWCNTs, and the lower band water-filled SWCNTs. All collected SWCNT populations were concentrated and adjusted toward a DOC concentration of 10 g/L using iterative concentration dilution cycles in a pressurized ultrafiltration stirred cell (Millipore) with either a 100 or 300 kDa MW cutoff membrane.

To begin ATPE separations from parent dispersions containing 10 g/L DOC without using direct dilution, which results in significant waste of materials and extra volume handling, two preconcentration (PC) steps were typically performed. In the first PC step, purified SWCNT sample (after either ultracentrifugation sorting or metal-semi separation) was first stepped to a 4 g/L DOC content by mixing 4 parts (by volume) parent dispersion with 4 parts 20% Dextran and 2 parts 25% PEG, generating a two-phase system in which all SWCNTs prefer the lower Dextran-rich phase. A second PC step was then typically performed to further lower the DOC content to 0.8–2 g/L and introduce SDS at approximately half of the desired concentration for the first separation, with the most typical step being based on a ratio of mixing approximately 1 part SWCNT to 3 parts 10% PEG/7.2% Dextran/0.6% SDS; all SWCNTs again remain in the lower phase. These PC steps are not explicitly necessary, but reduce consumption of solutions and in some cases remove hydrophobic (non-nanotube) impurities. After the two PC steps, the dextran-rich phase was then mixed with either top phase mimic (discussed next) and PEG/water to reach the desired surfactant concentration for first separation (0.4 g/L DOC, various SDS %) or in the case of metal-semi separations twice the volume of a stock solution containing 1.35% SC, 12.5% PEG, and 0.83% SDS, followed by an addition of 10  $\mu$ L/mL NaClO working solution.

Iterative diameter separation via ATPE was performed by the addition of known volumes of top phase or bottom phase mimic mixtures to the SWCNT-containing opposite phase. Aqueous mimic phase composition was 15–16% dextran, 0% PEG, 0.05% DOC, and 0% SDS for the bottom phase and 0% (mass/mass) dextran, 12.5% PEG, 0.4 g/L DOC, and X% SDS for the top phase mimic, in which X was varied depending on the desired SDS concentration delta; typical X values were 0.4%, 0.6%, and 1.2%. Iterative isolation of metallic and semiconducting nanotubes was performed as previously reported.<sup>8,42</sup> Final fractions were typically concentrated and pushed to the top, PEG-rich, phase to ease postprocessing and simplify optical measurements. For fractions in the top phase, postprocessing was performed by addition of bottom mimic phase and cooling to  $\sim$ 8 °C to partition all of the SWCNTs into the lower phase. To those fractions, along with fractions collected in the bottom phase, a small volume of top phase mimic (or PEG and SDS solutions) was added at an SDS concentration above that necessary to partition all species into the top phase. The ability to specify the relative volumes of each phase allows for the concentration of the SWCNTs. To ensure stability and enable optical measurements, an equal volume of 20 g/L DOC was added to each separated fraction. To perform additional separation steps on a finalized fraction to which DOC has been added, a sample can simply be treated as the initial parent dispersion and reprocessed back to partitioning conditions.

UV-vis-NIR absorbance spectra were collected on a Cary 5000 UV-vis-NIR spectrometer from 1880 to 185 nm in 1 nm increments through a 1 or 2 mm quartz cuvette with an integration time of 0.1 s/nm (2 nm slit width). The spectra of the corresponding blank surfactant solution were collected separately and linearly subtracted during data analysis.

Photoluminescence excitation contour maps were measured with a customized Thermo-Electron FT960 Raman spectrometer equipped with a Ge detector operating at 77 K. The excitation source was a 250 W tungsten-halogen bulb coupled to a single-grating monochromator, and the excitation intensity was  $<1$  mW. Samples were excited in 1 cm cuvettes in a front face configuration at an angle  $\gg 60^\circ$ . All spectra were corrected for intensity variations in the lamp spectrum, as well as for the responses of the system and detector.<sup>61</sup> Prior to fluorescence measurements, samples were exchanged into 10 g/L DOC in D<sub>2</sub>O using PEG precipitation<sup>62</sup> and dilution of the pellet with DOC-D<sub>2</sub>O solution by a factor of  $\sim 20\times$ .

Spontaneous Raman scatter was collected in a collinear 180° backscattering configuration on samples dispersed in DOC with a triple grating spectrometer (Horiba T64000) and a liquid nitrogen cooled CCD detector. An Ar<sup>+</sup> laser (Coherent Innova Sabre with single line visible head) provided excitation wavelengths of 458, 488, or 514 nm; in each case, approximately

25 mW of power was focused to a spot size of approximately 100  $\mu$ m within the liquid sample volume. For 603 and 654 nm excitation, 5 W of the Ar<sup>+</sup> laser was used to pump a dye laser (Kiton Red (620), Exciton), applying 20 mW of excitation to the sample volume. Benzonitrile was used in both cases as a reference standard to ensure wavenumber accuracy. Raman frequency shifts in the range from approximately 100 to 800 cm<sup>-1</sup> were measured, covering the RBM region of Raman shifts. The integration time per collection (each spectra was collected 3 $\times$ ) was between 10 and 60 s. After data collection, each spectrum was scaled by its integration time, and appropriate nonresonant background was subtracted (varied with excitation line): for 458, 488, or 514 nm all spectra at the same excitation wavelength were scaled by the same divisor; for 603 and 654 nm excitation the divisor varied as presented in Figure 8.

*Conflict of Interest:* The authors declare no competing financial interest.

*Acknowledgment.* E.H.H. and S.K.D. acknowledge partial support from the LANL-LDRD program. E.H.H. also gratefully acknowledges support from the LANL Director's Postdoctoral Fellowship. J.L.B. and R.I. graciously acknowledge support from the Solar Photochemistry Program of the U.S. Department of Energy, Office of Science, Basic Energy Sciences, Division of Chemical Sciences, Geosciences and Biosciences, under Contract No. DE-AC36-08GO28308 to NREL.

*Supporting Information Available:* Additional details of SWCNT preparation, separations on additional SWCNT populations, and additional optical characterization results are presented. This material is available free of charge via the Internet at <http://pubs.acs.org>.

## REFERENCES AND NOTES

- Tulevski, G. S.; Franklin, A. D.; Frank, D.; Lobe, J. M.; Cao, Q.; Park, H.; Afzali, A.; Han, S.; Hannon, J. B.; Haensch, W. Toward High-Performance Digital Logic Technology with Carbon Nanotubes. *ACS Nano* **2014**, *8*, 8730–8745.
- Sims, P. C.; Moody, I. S.; Choi, Y.; Dong, C.; Iftikhar, M.; Corso, B. L.; Gul, O. T.; Collins, P. G.; Weiss, G. A. Electronic Measurements of Single-Molecule Catalysis by cAMP-Dependent Protein Kinase A. *J. Am. Chem. Soc.* **2013**, *135*, 7861–7868.
- Kawai, M.; Kyakuno, H.; Suzuki, T.; Igashiki, T.; Suzuki, H.; Okazaki, T.; Kataura, H.; Maniwa, Y.; Yanagi, K. Single Chirality Extraction of Single-Wall Carbon Nanotubes for the Encapsulation of Organic Molecules. *J. Am. Chem. Soc.* **2012**, *134*, 9545–9548.
- Tyler, T. P.; Shastry, T. A.; Leever, B. J.; Hersam, M. C. Narrow Diameter Distributions of Metallic Arc Discharge Single-Walled Carbon Nanotubes via Dual-Iteration Density Gradient Ultra-centrifugation. *Adv. Mater.* **2012**, *24*, 4765–4768.
- Seo, J. T.; Yoder, N. L.; Shastry, T. A.; Humes, J. J.; Johns, J. E.; Green, A. A.; Hersam, M. C. Diameter Refinement of Semiconducting Arc Discharge Single-Walled Carbon Nanotubes via Density Gradient Ultracentrifugation. *J. Phys. Chem. Lett.* **2013**, *4*, 2805–2810.
- Albertsson, P. A. *Partition of Cell Particles and Macromolecules*, 2nd ed.; Wiley-Interscience: New York, NY, USA, 1971; pp 1–323.
- Zaslavsky, B. Y. *Aqueous Two-Phase Partitioning*; Marcel Dekker: New York, NY, USA, 1994; pp 1–696.
- Khrapin, C. Y.; Fagan, J. A.; Zheng, M. Spontaneous Partition of Carbon Nanotubes in Polymer-Modified Aqueous Phases. *J. Am. Chem. Soc.* **2013**, *135*, 6822–6825.
- Fagan, J. A.; Khrapin, C. Y.; Silvera Batista, C.; Simpson, J. R.; Házoz, E. H.; Hight Walker, A. R.; Zheng, M. Isolation of Specific Small-Diameter Single-Wall Carbon Nanotube Species via Aqueous Two-Phase Extraction. *Adv. Mater.* **2014**, *26*, 2800–2804.
- Zhang, M.; Khrapin, C. Y.; Fagan, J. A.; McPhie, P.; Ito, Y.; Zheng, M. Single-Step Total Fractionation of Single-Wall Carbon Nanotubes by Countercurrent Chromatography. *Anal. Chem.* **2014**, *86*, 3980–3984.

11. Gu, T. Liquid-Liquid Partitioning Methods for Bioseparations. In *The Handbook of Bioseparations*; Ahuja, S., Ed.; Academic Press: New York, NY, USA, 2000; pp 329–364.
12. Helfrich, M. R.; El-Kouedi, M.; Etherton, M. P.; Keating, C. D. Partitioning and Assembly of Metal Particles and Their Bioconjugates in Aqueous Two-Phase Systems. *Langmuir* **2005**, *21*, 8478–8486.
13. Wenseleers, W.; Vlasov, I. I.; Goovaerts, E.; Obraztsova, E.; Lobach, A. S.; Bouwen, A. Efficient Isolation and Solubilization of Pristine Single-Walled Nanotubes in Bile Salt Micelles. *Adv. Funct. Mater.* **2004**, *14*, 1105–1112.
14. Weisman, R. B.; Bachilo, S. M. Dependence of Optical Transition Energies on Structure for Single-Walled Carbon Nanotubes in Aqueous Suspension: An Empirical Kataura Plot. *Nano Lett.* **2003**, *3*, 1235–1238.
15. Ao, G.; Khrapin, C. Y.; Zheng, M. DNA-Controlled Partition of Carbon Nanotubes in Polymer Aqueous Two-Phase Systems. *J. Am. Chem. Soc.* **2014**, *136*, 10383–10392.
16. Cambré, S.; Schoeters, B.; Luyckx, S.; Goovaerts, E.; Wenseleers, W. Experimental Observation of Single-File Water Filling of Thin Single-Wall Carbon Nanotubes Down to Chiral Index (5,3). *Phys. Rev. Lett.* **2010**, *104*, 207401.
17. Arnold, M. S.; Stupp, S. I.; Hersam, M. C. Enrichment of Single-Walled Carbon Nanotubes by Diameter in Density Gradients. *Nano Lett.* **2005**, *5*, 713–718.
18. Arnold, M. S.; Green, A. A.; Hulvat, J. F.; Stupp, S. I.; Hersam, M. C. Sorting Carbon Nanotubes by Electronic Structure Using Density Differentiation. *Nat. Nanotechnol.* **2006**, *1*, 60–65.
19. Yanagi, K.; Miyata, Y.; Kataura, H. Optical and Conductive Characteristics of Metallic Single-Wall Carbon Nanotubes with Three Basic Colors; Cyan, Magenta, and Yellow. *Appl. Phys. Express* **2008**, *1*, 034003.
20. Ghosh, S.; Bachilo, S. M.; Weisman, R. B. Advanced Sorting of Single-Walled Carbon Nanotubes by Nonlinear Density-Gradient Ultracentrifugation. *Nat. Nanotechnol.* **2010**, *5*, 443–450.
21. Niyogi, S.; Densmore, C. G.; Doorn, S. K. Electrolyte Tuning of Surfactant Interfacial Behavior for Enhanced Density-Based Separations of Single-Walled Carbon Nanotubes. *J. Am. Chem. Soc.* **2009**, *131*, 1144–1153.
22. Hároz, E. H.; Rice, W. D.; Lu, B. Y.; Ghosh, S.; Hauge, R. H.; Weisman, R. B.; Doorn, S. K.; Kono, J. Enrichment of Armchair Carbon Nanotubes via Density Gradient Ultracentrifugation: Raman Spectroscopy Evidence. *ACS Nano* **2010**, *4*, 1955–1962.
23. Cambré, S.; Wenseleers, W. Separation and Diameter-Sorting of Empty (End-Capped) and Water-Filled (Open) Carbon Nanotubes by Density Gradient Ultracentrifugation. *Angew. Chem., Int. Ed.* **2011**, *50*, 2764–2768.
24. Liu, J.; Hersam, M. C. Recent Developments in Carbon Nanotube Sorting and Selective Growth. *MRS Bull.* **2010**, *35*, 315–321.
25. Zheng, M.; Jagota, A.; Semke, E. D.; Diner, B. A.; McLean, R. S.; Lustig, S. R.; Richardson, R. E.; Tassi, N. G. DNA-Assisted Dispersion and Separation of Carbon Nanotubes. *Nat. Mater.* **2003**, *2*, 338–342.
26. Tu, X.; Manohar, A.; Jagota, A.; Zheng, M. DNA Sequence Motifs for Structure Specific Recognition and Separation of Carbon Nanotubes. *Nature* **2009**, *460*, 250–253.
27. Tu, X.; Hight Walker, A. R.; Khrapin, C. Y.; Zheng, M. Evolution of DNA Sequences toward Recognition of Metallic Armchair Carbon Nanotubes. *J. Am. Chem. Soc.* **2011**, *133*, 12998–13001.
28. Liu, H. P.; Nishide, D.; Tanaka, T.; Kataura, H. Large-Scale Single-Chirality Separation of Single-Wall Carbon Nanotubes by Simple Gel Chromatography. *Nat. Commun.* **2011**, *2*, 309–317.
29. Liu, H.; Tanaka, T.; Urabe, Y.; Kataura, H. High-Efficiency Single-Chirality Separation of Carbon Nanotubes Using Temperature-Controlled Gel Chromatography. *Nano Lett.* **2013**, *13*, 1996–2003.
30. Flavel, B. S.; Kappes, M. M.; Krupke, R.; Hennrich, F. Separation of Single-Walled Carbon Nanotubes by 1-Dodecanol-Mediated Size-Exclusion Chromatography. *ACS Nano* **2013**, *7*, 3557–3564.
31. Jain, R. M.; Tvrdy, K.; Han, R.; Ulissi, Z.; Strano, M. S. Quantitative Theory of Adsorptive Separation for the Electronic Sorting of Single-Walled Carbon Nanotubes. *ACS Nano* **2014**, *8*, 3367–3379.
32. Silvera-Batista, C. A.; Scott, D. C.; Mcleod, S. M.; Ziegler, K. J. A Mechanistic Study of the Selective Retention of SDS-Suspended Single-Wall Carbon Nanotubes on Agarose Gels. *J. Phys. Chem. C* **2011**, *115*, 9361–9369.
33. Ihara, K.; Endoh, H.; Saito, T.; Nihey, F. Separation of Metallic and Semiconducting Single-Wall Carbon Nanotube Solution by Vertical Electric Field. *J. Phys. Chem. C* **2011**, *115*, 22827–22832.
34. Nish, A.; Hwang, J.; Doig, J.; Nicholas, R. J. Highly Selective Dispersion of Single-Walled Carbon Nanotubes Using Aromatic Polymers. *Nat. Nanotechnol.* **2007**, *2*, 640–646.
35. Mistry, K. S.; Larsen, B. A.; Blackburn, J. L. High-Yield Dispersions of Large-Diameter Semiconducting Single-Walled Carbon Nanotubes with Tunable Narrow Chirality Distributions. *ACS Nano* **2013**, *7*, 2231–2239.
36. Subbaiyan, N. K.; Parra-Vasquez, A. N. G.; Cambré, S.; Santiago Cordoba, M. A.; Yalcin, S. E.; Hamilton, C. E.; Mack, N. H.; Blackburn, J. L.; Doorn, S. K.; Duque, J. G. Benchtop Aqueous Two-Phase Extraction of Isolated Individual Single-Walled Carbon Nanotubes. *Nano Res.* DOI 10.1007/s12274-014-0680-z.
37. Fagan, J. A.; Huh, J. Y.; Simpson, J. R.; Blackburn, J. L.; Holt, J. M.; Larsen, B. A.; Walker, A. R. H. Separation of Empty and Water-Filled Single-Wall Carbon Nanotubes. *ACS Nano* **2011**, *5*, 3943–3953.
38. Khrapin, C. Y.; Tu, X.; Heddleston, J. M.; Silvera-Batista, C.; Hight Walker, A. R.; Fagan, J.; Zheng, M. High-Resolution Length Fractionation of Surfactant-Dispersed Carbon Nanotubes. *Anal. Chem.* **2013**, *85*, 1382–1388.
39. Moore, V. C.; Strano, M. S.; Haroz, E. H.; Hauge, R. H.; Smalley, R. E.; Schmidt, J.; Talmon, Y. Individually Suspended Single-Walled Carbon Nanotubes in Various Surfactants. *Nano Lett.* **2003**, *3*, 1379–1382.
40. Subbaiyan, N. K.; Cambré, S.; Parra-Vasquez, A. N. G.; Hároz, E. H.; Doorn, S. K.; Duque, J. G. Role of Surfactants and Salt in Aqueous Two-Phase Separation of Carbon Nanotubes toward Simple Chirality Isolation. *ACS Nano* **2014**, *8*, 1619–1628.
41. Abbott, N. L.; Blankschtein, D.; Hatton, T. A. Protein Partitioning in Two-Phase Aqueous Polymer Systems. 5. Decoupling of the Effects of Protein Concentration, Salt Type, and Polymer Molecular Weight. *Macromolecules* **1993**, *26*, 825–828.
42. Hui, G.; Streit, J. K.; Fagan, J. A.; Walker, A. R. H.; Zhou, C.; Zheng, M. Redox Sorting of Carbon Nanotubes. *Nano Lett.* **2015**, *15*, 1642–1646.
43. Hároz, E. H.; Duque, J. G.; Lu, B. Y.; Nikolaev, P.; Arepalli, S.; Hauge, R. H.; Doorn, S. K.; Kono, J. Unique Origin of Colors of Armchair Carbon Nanotubes. *J. Am. Chem. Soc.* **2012**, *134* (10), 4461–4464.
44. Vos, J. J. Colorimetric and Photometric Properties of a 2-deg Fundamental Observer. *Color Res. Appl.* **1978**, *3*, 125–135.
45. Streit, J. K.; Bachilo, S. M.; Ghosh, S.; Lin, C.; Weisman, R. B. Directly Measured Optical Absorption Cross Sections for Structure-Selected Single-Walled Carbon Nanotubes. *Nano Lett.* **2014**, *14*, 1530–1536.
46. Tsyboulski, D. A.; Rocha, J. R.; Bachilo, S. M.; Cognet, L.; Weisman, R. B. Structure-Dependent Fluorescence Efficiencies of Individual Single-Walled Carbon Nanotubes. *Nano Lett.* **2007**, *7*, 3080–3085.
47. Maultzsch, J.; Telg, H.; Reich, S.; Thomsen, C. Radial Breathing Mode of Single-Walled Carbon Nanotubes: Optical Transition Energies and Chiral-Index Assignment. *Phys. Rev. B* **2005**, *72*, 205438.
48. White, C. T.; Todorov, T. N. Carbon Nanotubes as Long Ballistic Conductors. *Nature* **1998**, *393*, 240–242.
49. Woods, L. M.; Mahan, G. D. Electron-Phonon Effects in Graphene and Armchair (10,10) Single-Wall Carbon Nanotubes. *Phys. Rev. B* **2000**, *61*, 10651–10663.
50. Striolo, A.; Chialvo, A. A.; Gubbins, K. E.; Cummings, P. T. Water in Carbon Nanotubes: Adsorption Isotherms and

- Thermodynamic Properties from Molecular Simulation. *J. Chem. Phys.* **2005**, *122*, 234712.
51. Volkov, A. N.; Zhigilei, L. V. Structural Stability of Carbon Nanotube Films: The Role of Bending Buckling. *ACS Nano* **2010**, *4*, 6187–6195.
52. Finnie, P.; Ding, J.; Li, Z.; Kingston, C. T. Assessment of the Metallicity of Single-Wall Carbon Nanotube Ensembles at High Purities. *J. Phys. Chem. C* **2014**, *118*, 30127–30138.
53. Telg, H.; Hároz, E. H.; Duque, J. G.; Tu, X.; Khripin, C. Y.; Fagan, J. A.; Zheng, M.; Kono, J.; Doorn, S. K. Diameter Dependence of TO Phonon Frequencies and the Kohn Anomaly in Armchair Single-Wall Carbon Nanotubes. *Phys. Rev. B* **2014**, *90*, 245422.
54. Ding, J.; Li, Z.; Lefebvre, J.; Cheng, F.; Dubey, G.; Zou, S.; Finnie, P.; Hrdina, A.; Scsoles, L.; Lopinski, G. P.; et al. Enrichment of Large-Diameter Semiconducting SWCNTs by Polyfluorene Extraction for High Network Density Thin Film Transistors. *Nanoscale* **2014**, *6*, 2328–2339.
55. Cheng, H. M.; Li, F.; Su, G.; Pan, H. Y.; He, L. L.; Sun, X.; Dresselhaus, M. S. Large-Scale and Low-Cost Synthesis of Single-Walled Carbon Nanotubes by the Catalytic Pyrolysis of Hydrocarbons. *Appl. Phys. Lett.* **1998**, *72*, 3282–3284.
56. Yu, B.; Liu, C.; Hou, P.; Tian, Y.; Li, S.; Liu, B.; Li, F.; Kauppinen, E. I.; Cheng, H. M. Bulk Synthesis of Large Diameter Semiconducting Single-Walled Carbon Nanotubes by Oxygen-Assisted Floating Catalyst Chemical Vapor Deposition. *J. Am. Chem. Soc.* **2011**, *133*, 5232–5235.
57. Arnold, M. S.; Suntivich, J.; Stupp, S. I.; Hersam, M. C. Hydrodynamic Characterization of Surfactant Encapsulated Carbon Nanotubes Using an Analytical Ultracentrifuge. *ACS Nano* **2008**, *2*, 2291–2300.
58. Fagan, J. A.; Zheng, M.; Rastogi, V.; Simpson, J. R.; Khripin, C. Y.; Silvera Batista, C. A.; Hight Walker, A. R. Analyzing Surfactant Structures on Length and Chirality Resolved (6,5) Single-Wall Carbon Nanotubes by Analytical Ultracentrifugation. *ACS Nano* **2013**, *7*, 3373–3387.
59. Blanch, A. J.; Shapter, J. G. Surfactant Concentration Dependent Spectral Effects of Oxygen and Depletion Interactions in Sodium Dodecyl Sulfate Dispersions of Carbon Nanotubes. *J. Phys. Chem. B* **2014**, *118*, 6288–6296.
60. Arnold, M. S.; Blackburn, J. L.; Crochet, J. J.; Doorn, S. K.; Duque, J. G.; Mohite, A.; Telg, H. Recent Developments in the Photophysics of Single-Walled Carbon Nanotubes for Their Use as Active and Passive Material Elements in Thin Film Photovoltaics. *Phys. Chem. Chem. Phys.* **2013**, *15*, 14896–14918.
61. McDonald, T. J.; Jones, M.; Engtrakul, C.; Ellingson, R. J.; Rumbles, G.; Heben, M. J. Near-Infrared Fourier Transform Photoluminescence Spectrometer with Tunable Excitation for the Study of Single-Walled Carbon Nanotubes. *Rev. Sci. Instrum.* **2006**, *77*, 053104.
62. Khripin, C. Y.; Arnold-Medabalimi, N.; Zheng, M. Molecular Crowding-Induced Clustering of DNA-Wrapped Carbon Nanotubes for Facile Length Fractionation. *ACS Nano* **2011**, *5*, 8258–8266.